The Astrophysical Journal, 910:141 (11pp), 2021 April 1 https://doi.org/10.3847/1538-4357/abe854


# Carbon-chain Chemistry versus Complex-organic-molecule Chemistry in Envelopes around Three Low-mass Young Stellar Objects in the Perseus Region

Kotomi Taniguchi[1], Liton Majumdar[2], Shigehisa Takakuwa[3], Masao Saito[4,5], Dariusz C. Lis[6], Paul F. Goldsmith[6], and Eric Herbst[7,8]

[1] Department of Physics, Faculty of Science, Gakushuin University, Mejiro, Toshima, Tokyo 171-8588, Japan; kotomi.taniguchi@gakushuin.ac.jp
[2] School of Earth and Planetary Sciences, National Institute of Science Education and Research, HBNI, Jatni 752050, Odisha, India; liton@niser.ac.in
[3] Department of Physics and Astronomy, Graduate School of Science and Engineering, Kagoshima University, 1-21-35 Korimoto, Kagoshima, Kagoshima 890-0065, Japan
[4] National Astronomical Observatory of Japan (NAOJ), National Institutes of Natural Sciences, Osawa, Mitaka, Tokyo 181-8588, Japan
[5] Department of Astronomical Science, School of Physical Science, SOKENDAI (The Graduate University for Advanced Studies), Osawa, Mitaka, Tokyo 181-8588, Japan
[6] Jet Propulsion Laboratory, California Institute of Technology, 48010 Oak Grove Drive, Pasadena, CA 91109, USA
[7] Department of Astronomy, University of Virginia, Charlottesville, VA 22904, USA
[8] Department of Chemistry, University of Virginia, Charlottesville, VA 22903, USA
*Received 2021 January 4; revised 2021 February 15; accepted 2021 February 19; published 2021 April 6*

## Abstract

We have analyzed ALMA Cycle 5 data in Band 4 toward three low-mass young stellar objects, IRAS 03235+3004 (hereafter IRAS 03235), IRAS 03245+3002 (IRAS 03245), and IRAS 03271+3013 (IRAS 03271), in the Perseus region. The $HC_3N$ ($J = 16$–$15$; $E_{up}/k = 59.4$ K) line has been detected in all of the target sources, while four $CH_3OH$ lines ($E_{up}/k = 15.4$–$36.3$ K) have been detected only in IRAS 03245. Sizes of the $HC_3N$ distributions (∼2930–3230 au) in IRAS 03235 and IRAS 03245 are similar to those of the carbon-chain species in the warm carbon-chain chemistry (WCCC) source L1527. The size of the $CH_3OH$ emission in IRAS 03245 is ∼1760 au, which is slightly smaller than that of $HC_3N$ in this source. We compare the $CH_3OH/HC_3N$ abundance ratios observed in these sources with predictions of chemical models. We confirm that the observed ratio in IRAS 03245 agrees with the modeled values at temperatures around 30–35 K, which supports the $HC_3N$ formation by the WCCC mechanism. In this temperature range, $CH_3OH$ does not thermally desorb from dust grains. Nonthermal desorption mechanisms or gas-phase formation of $CH_3OH$ seem to work efficiently around IRAS 03245. The fact that IRAS 03245 has the highest bolometric luminosity among the target sources seems to support these mechanisms, in particular the nonthermal desorption mechanisms.

*Unified Astronomy Thesaurus concepts:* Astrochemistry (75); Interstellar molecules (849); Low mass stars (2050)

## 1. Introduction

Studying the environment and evolution of low-mass star-forming regions is important for revealing how our Sun was born. The chemical composition in star-forming regions provides us various information, for example, evolutionary stages and physical conditions (e.g., Caselli & Ceccarelli 2012).

The gas-phase chemical composition around young stellar objects (YSOs) yields essential information on not just the current evolutionary stage but also former environments or evolutionary processes in the pre-stellar core phase (Sakai & Yamamoto 2013; Spezzano et al. 2016; Taniguchi et al. 2019a, 2020). The ice mantles form in cold and dense starless cores. Although saturated complex organic molecules (COMs) were considered to be deficient in the gas phase during the cold stage, several COMs have now been detected in starless cores, e.g., the Barnard 5 cold dark cloud (Taquet et al. 2017) and the L1544 pre-stellar core (Jiménez-Serra et al. 2016). These COMs are considered to be formed in the gas phase (e.g., Balucani et al. 2015) or formed on dust surfaces followed by nonthermal desorption mechanisms. New dust-surface mechanisms proposed by Jin & Garrod (2020) successfully reproduce observed abundances of COMs in the L1544 pre-stellar core. Furthermore, modeling studies including radiolysis can also produce high COM abundances (e.g., Shingledecker & Herbst 2018; Shingledecker et al. 2018; Paulive et al. 2021). Hence, even in cold dense cores, chemical processes forming COMs are also efficient. After YSOs are born, ice mantles, including COMs, sublimate when the temperature rises to ≈100 K. The chemistry in YSOs then strongly depends on their density and temperature structures (e.g., Jørgensen et al. 2020, and therein).

There are two, well-recognized chemical processes effective around low-mass YSOs. One is hot corino chemistry, in which saturated COMs are abundant in the hot (>100 K) dense ($\geqslant 10^7$ cm$^{-3}$) gas (Ceccarelli 2004; Herbst & van Dishoeck 2009). Hot corino chemistry is initiated by successive hydrogenation reactions of CO molecules on grain surfaces to form $CH_3OH$, which is a fundamental COM and a precursor of more complex COMs (Öberg & Bergin 2021). The other is warm carbon-chain chemistry (WCCC; Sakai & Yamamoto 2013). Carbon-chain molecules are formed from gaseous $CH_4$, which is one of the main constituents of ice mantles (Öberg & Bergin 2021), in lukewarm envelopes (≈25–35 K, Hassel et al. 2008). Hence, the presence of two types of chemistry around low-mass YSOs may indicate that some conditions of the pre-stellar core phase produce CO-rich ice and others lead to $CH_4$-rich ice. However, the origin of the chemical diversity is still controversial. The results of this paper will help to explain the chemical diversity.

Although COMs are generally considered to be abundant in hot dense gas around YSOs, a recent survey observation has revealed that $CH_3OH$ and $CH_3CHO$ are prevalent. Scibelli & Shirley (2020)

**Table 1**
Summary of Target Sources

| Source Name | R.A. (J2000)[a] | Decl. (J2000)[a] | $T_{bol}$ (K)[b] | $L_{bol}$ ($L_\odot$)[c] | $M_{env}$ ($M_\odot$)[d] | $\alpha$[b] | Class[e] | $T_{dust}$ (K)[f] |
|---|---|---|---|---|---|---|---|---|
| IRAS 03235+3004 | $03^h26^m37\overset{s}{.}45$ | $+30°15'27\overset{''}{.}9$ | 73 | 1.29 | $0.69 \pm 0.11$ | 1.03 | 0 | ... |
| IRAS 03245+3002 | $03^h27^m39\overset{s}{.}03$ | $+30°12'59\overset{''}{.}3$ | 65 | 4.94 | $0.70 \pm 0.04$ | 2.46 | 0 | $37 \pm 2$ |
| IRAS 03271+3013 | $03^h30^m15\overset{s}{.}16$ | $+30°23'48\overset{''}{.}8$ | 100 | 2.06 | $0.63 \pm 0.10$ | 1.58 | I | $45 \pm 2$ |

**Notes.**
[a] Coordinates of the phase reference centers.
[b] Bolometric temperature taken from Dunham et al. (2015).
[c] Bolometric luminosities at an assumed distance of 250 pc taken from Dunham et al. (2015) are scaled to the newly measured distance of Perseus (293 pc; Ortiz-León et al. 2018).
[d] Envelope masses at an assumed distance of 250 pc taken from Enoch et al. (2009) are scaled to the newly measured distance of Perseus (293 pc).
[e] IR spectral indexes ($\alpha$) taken from Enoch et al. (2009).
[f] Dust temperatures taken from Emprechtinger et al. (2009).

conducted survey observations of these COMs toward 31 starless cores in the Taurus region with the Arizona Radio Observatory (ARO) 12 m telescope, and reported that the detection fractions of $CH_3OH$ and $CH_3CHO$ are 100% (31/31) and 70% (22/31), respectively. It was also found that the $CH_3OH$ abundance decreases from young cores to evolved starless cores possibly due to depletion onto dust grains (Scibelli & Shirley 2020). The detection of COMs in the starless cores suggests that there are some nonthermal desorption mechanisms or efficient gas-phase formation pathways at work in starless cores.

Takakuwa et al. (1998) showed different spatial distributions of $H^{13}CO^+$ and $CH_3OH$ in the TMC-1C region and suggested that $CH_3OH$ cores are younger and farther from protostar formation than $H^{13}CO^+$ cores. A subsequent study supports the possibility of the different evolutionary stages of these cores (Takakuwa et al. 2003a). Furthermore, Takakuwa et al. (2000) carried out mapping observations toward the Heiles Cloud 2 region in Taurus and found that the $CH_3OH$ emission is weak toward the protostars (Class 0 and Class I) and rather stronger toward cores without protostars. Takakuwa et al. 2003b also conducted mapping observations toward IRAS 04191+1522, a very young Class 0 YSO. They found that the $CH_3OH$ abundance toward the YSO is ~10 times lower than that toward the interaction region between the outflow and the surrounding dense gas. Similar observational results of the nondetection or weak emission of $CH_3OH$ at protostellar positions have been reported (e.g., White et al. 2006). The weak $CH_3OH$ emission at protostellar cores has been reported even in the higher angular-resolution observations with ALMA at 3 mm, where the obscuring effect by the dust emission is not significant (Maureira et al. 2020). All these observational results imply that $CH_3OH$ is associated with young starless cores and adsorbed onto dust grains in evolved starless cores. The weak $CH_3OH$ emission toward low-mass YSOs (Takakuwa et al. 2000, 2003b; White et al. 2006; Maureira et al. 2020) probably indicates that $CH_3OH$ lines are not necessarily tracers for low-mass protostellar cores, and not all the protostellar sources possess hot core/hot corinos.

Cyanoacetylene ($HC_3N$), which is the shortest member of the cyanopolyyne family ($HC_{2n+1}N$), is known to be abundant in starless cores, as well as other carbon-chain species (e.g., Suzuki et al. 1992). It is also detected around low-mass and high-mass YSOs (Law et al. 2018; Taniguchi et al. 2018, 2019b), and protoplanetary disks (Öberg et al. 2015; Bergner et al. 2018). Hence, $HC_3N$ is prevalent in star-forming regions in various evolutionary stages. However, it has not been determined whether the WCCC mechanism is responsible for formation of $HC_3N$ around low-mass YSOs, because there is no information about spatial distributions of $HC_3N$ around these sources at sufficiently high spatial resolutions (Law et al. 2018).

**Table 2**
Summary of Spectral Windows Covered by the Correlator Setup

| Frequency Range (GHz) | Frequency Res. (kHz) | Angular Resolution | Molecular Lines |
|---|---|---|---|
| 147.097–147.224 | 124 | $11\overset{''}{.}0 \times 8\overset{''}{.}6$ | Continuum |
| 145.526–145.591 | 121 | $11\overset{''}{.}2 \times 8\overset{''}{.}4$ | $HC_3N$ |
| 157.236–157.301 | 121 | $10\overset{''}{.}6 \times 8\overset{''}{.}2$ | $CH_3OH$ |

In the present paper, we focus on methanol and cyanoacetylene as potential indicators to constrain evolutionary stages of low-mass YSOs. For this purpose, high angular-resolution imaging observations of $CH_3OH$ and $HC_3N$ in low-mass YSOs are essential. We investigate the spatial distributions of $HC_3N$ and $CH_3OH$ toward three low-mass YSOs, IRAS 03235+3004 (hereafter IRAS 03235), IRAS 03245+3002 (IRAS 03245), and IRAS 03271+3013 (IRAS 03271), in the Perseus region, using ALMA archival data. In Section 2, we will describe the used data and reduction procedures. The resultant continuum images, moment 0 maps, and spectra of $HC_3N$ and $CH_3OH$ are shown in Section 3. The observed $CH_3OH/HC_3N$ abundance ratio is compared with the results of the chemical network simulations in Section 4. Finally, we summarize our main conclusions in Section 5.

## 2. Data Reduction

In this paper, we present ALMA Band 4 archival data toward three low-mass YSOs in the Perseus region taken from Cycle 5 data.[9] The properties of our target sources are summarized in Table 1. In Table 1, the coordinates correspond to the phase reference centers of these ALMA observations carried out with the 7 m Array in 2018 July.

Table 2 summarizes information concerning each spectral window presented in this paper. We used the first spectral window for continuum data. The second and third windows contain lines of $HC_3N$ and $CH_3OH$, respectively. Observed lines of each molecule are summarized in Table 3. The frequency resolution of 121 kHz corresponds to a velocity

[9] project ID; 2017.1.00955.S, PI; Jennifer Bergner.

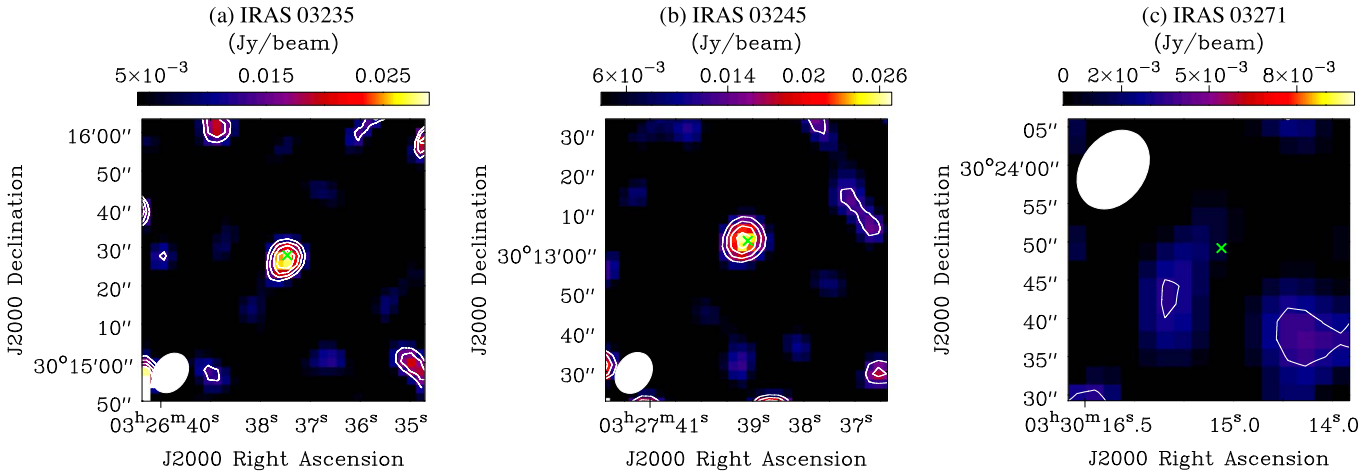


**Figure 1.** Continuum images toward the three IRAS sources. The contour levels are $3\sigma$, $4\sigma$, $5\sigma$, and $6\sigma$ of the rms noise levels. In panel (c), only the $3\sigma$ level contour appears. The noise levels are 4 mJy beam$^{-1}$ for panels (a) and (b), and 1 mJy beam$^{-1}$ for panel (c), respectively. The filled white ellipses indicate the angular resolution of approximately $11\farcs0 \times 8\farcs6$. The crosses indicate source positions taken from the Spitzer c2d program (Enoch et al. 2009).

**Table 3**
Summary of Target Molecular Lines

| Molecule | Transition | Frequency (GHz) | $E_{up}/k$ (K) | $\log_{10}(A_{ij})$ ($s^{-1}$) |
|---|---|---|---|---|
| $HC_3N$ | 16–15 | 145.560946 | 59.4 | −3.61727 |
| $CH_3OH$ | $4_0 - 4_{-1}$ $E_2$ | 157.246062 | 36.3 | −4.67809 |
| | $1_0 - 1_{-1}$ $E_2$ | 157.270832 | 15.4 | −4.65644 |
| | $3_0 - 3_{-1}$ $E_2$ | 157.272338 | 27.1 | −4.66831 |
| | $2_0 - 2_{-1}$ $E_2$ | 157.276019 | 20.1 | −4.66116 |

**Note.** Taken from the Jet Propulsion Laboratory (JPL) catalog (Pickett et al. 1998).

resolution of ∼0.24 km s$^{-1}$. The field of view (FoV) and largest angular scale (LAS) are 65.″3 and 43.″6, respectively.

We carried out data reduction and imaging using the Common Astronomy Software Application (CASA v 5.4.0; McMullin et al. 2007) on the pipeline-calibrated visibilities. The data cubes were created with the CASA tclean task. Uniform weighting was applied. The resulting angular resolution of $\sim 11'' \times 8''$ corresponds to ∼0.016 pc × 0.011 pc (∼3220au × 2340au) at the source distance (293 pc; Ortiz-León et al. 2018). The pixel size and image size are 2.″3 and 250 × 250 pixels.

Continuum ($\lambda = 2$ mm) images were created from the data cubes using the IMCONTSUB task. The noise levels of the continuum images are 4 mJy beam$^{-1}$ in IRAS 03235 and IRAS 03245, and 1 mJy beam$^{-1}$ in IRAS 03271, respectively.

## 3. Results and Analyses

### 3.1. Results: Spatial Distributions

Figure 1 shows the continuum images of the three target sources. The green crosses indicate positions of infrared sources revealed by the Spitzer Core to Disk (c2d) Legacy program (Evans et al. 2003; Enoch et al. 2009). In IRAS 03235 and IRAS 03245, the dust continuum peaks are consistent with the Spitzer sources. On the other hand, the detection of dust continuum emission is not significant in IRAS 03271.

The $HC_3N$ ($J = 16 - 15$) line has been detected in all of the sources, and panels (a)–(c) of Figure 2 show moment 0 maps of $HC_3N$ toward the three sources. Methanol ($CH_3OH$) has been detected only in IRAS 03245. We used two lines ($1_0 - 1_{-1}$ and $3_0 - 3_{-1}$) for making the $CH_3OH$ moment 0 map, because these lines are partially blended. Panel (d) of Figure 2 shows its moment 0 map toward IRAS 03245.

Since all of the target sources have similar envelope masses (Table 1), the detection/nondetection of $CH_3OH$ does not likely depend on the presence of an envelope. Graninger et al. (2016a) detected $CH_3OH$ toward all of the three sources with the IRAM 30 m telescope with a beam size of ∼25″. In their observations, only two lines with low upper-state energies ($E_{up}/k = 6.97$ K and 12.54 K) were detected as weak lines in IRAS 03235 and IRAS 03271. The noise levels of the ACA 7 m observations could be too high to detect weak lines of $CH_3OH$ in IRAS 03235 and IRAS 03271.

We applied 2D Gaussian fitting to the continuum and moment 0 maps. The fit results are summarized in Table 4. In the case that beam-deconvolved sizes could not be obtained, we indicate the synthesized beam as their upper limits.

In IRAS 03235, the peak position of $HC_3N$ is consistent with that of the continuum image as well as the Spitzer source. The size of the $HC_3N$ emission (∼11″, corresponding to ∼3223 au) may be slightly larger than that of the continuum, as also seen in panel (a) of Figure 2. The extent of the $HC_3N$ emission (∼3223 au) is similar to the size of spatial distributions of carbon-chain species in L1527 in the Taurus region (Sakai et al. 2010). Thus, $HC_3N$ is likely to be efficiently formed in moderate temperature regions (∼25–35 K) by the WCCC (Sakai & Yamamoto 2013) mechanism.

In IRAS 03245, the peak positions of dust continuum and $CH_3OH$ are consistent with the Spitzer point source. The spatial extent of $HC_3N$ (≈10″, ∼2930 au) is similar to that in IRAS 03235 (∼3223 au). Again, the WCCC mechanism could contribute to formation of $HC_3N$. The emission region of $HC_3N$ is larger than that of $CH_3OH$ (∼6″, corresponding to ∼1758 au). These features can be seen in panels (b) and (d) of Figure 2.

The peak position of $HC_3N$ emission is not consistent with the Spitzer point source, but is located ∼1470 au to the east of it. The origins of such discrepancies are not clear at the current angular resolution. One possibility is that $HC_3N$ emission is associated with the molecular outflow, because the direction of the offset of the $HC_3N$ emission peak from the Spitzer source is

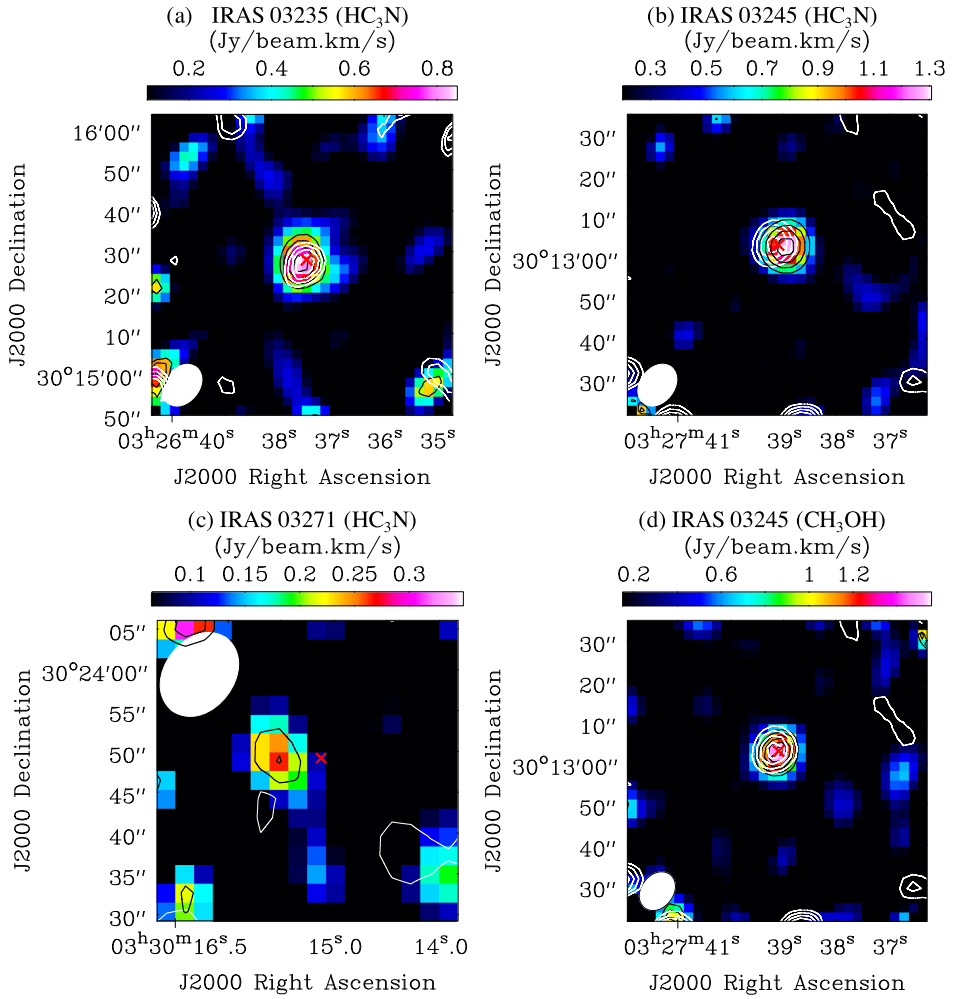


**Figure 2.** Moment 0 maps of (a)–(c) $HC_3N$ and (d) $CH_3OH$. The black contour levels are $5\sigma$, $6\sigma$, $7\sigma$, and $8\sigma$ for panels (a) and (d), and $3\sigma$, $4\sigma$, $5\sigma$, and $6\sigma$ for panels (b) and (c), respectively. In panel (c), only the $3\sigma$ and $4\sigma$ level contours appear. The noise levels are 0.1, 0.2, 0.065, and 0.15 Jy beam$^{-1}\times$ km s$^{-1}$ for panels (a)–(d), respectively. The white contours show the distribution of dust continuum emissions, as in Figure 1. The filled white ellipses represent an angular resolution of approximately $11\farcs2 \times 8\farcs4$ for panels (a)–(c) and $10\farcs6 \times 8\farcs2$ for panel (d). The crosses indicate source positions from the Spitzer c2d program (Enoch et al. 2009).

**Table 4**
Results of 2D Gaussian Fitting

| Source | Species | Peak Position (J2000) | Size | Position Angle | Peak Intensity[a] |
|---|---|---|---|---|---|
| IRAS 03235 | continuum | $03^h26^m37\overset{s}{.}507 \pm 0\overset{s}{.}013$, $+30°15'26\farcs81 \pm 0\farcs20$ | $<11\farcs0 \times 8\farcs5$ | ⋯ | $33.0 \pm 1.7$ |
| | $HC_3N$ | $03^h26^m37\overset{s}{.}498 \pm 0\overset{s}{.}025$, $+30°15'27\farcs83 \pm 0\farcs36$ | $11\farcs5 \pm 1\farcs5 \times 8\farcs6 \pm 2\farcs0$ | 39° | $0.839 \pm 0.047$ |
| IRAS 03245 | continuum | $03^h27^m39\overset{s}{.}171 \pm 0\overset{s}{.}016$, $+30°13'03\farcs28 \pm 0\farcs23$ | $<11\farcs0 \pm \times 8\farcs6$ | ⋯ | $30.1 \pm 1.7$ |
| | $HC_3N$ | $03^h27^m38\overset{s}{.}971 \pm 0\overset{s}{.}018$, $+30°13'02\farcs57 \pm 0\farcs21$ | $9\farcs92 \pm 0\farcs89 \times 2\farcs83 \pm 2\farcs53$ | 55° | $1.306 \pm 0.054$ |
| | $CH_3OH$ | $03^h27^m39\overset{s}{.}129 \pm 0\overset{s}{.}010$, $+30°13'02\farcs60 \pm 0\farcs14$ | $5\farcs82 \pm 0\farcs78 \times 1\farcs25 \pm 1\farcs64$ | 49° | $1.659 \pm 0.051$ |
| IRAS 03271 | $HC_3N$ | $03^h30^m15\overset{s}{.}494 \pm 0\overset{s}{.}025$, $+30°23'49\farcs18 \pm 0\farcs63$ | $<11\farcs1 \times 8\farcs5$ | ⋯ | $0.305 \pm 0.035$ |

**Note.**
[a] Units for peak intensity are "mJy beam$^{-1}$" and "Jy beam$^{-1}\times$ km s$^{-1}$" for continuum and the molecular emissions, respectively.

similar to the direction of the molecular outflow (Hsieh et al. 2019).

### 3.2. Spectral Analyses

Figures 3 and 4 show spectra of $HC_3N$ and $CH_3OH$ at the $HC_3N$ emission peaks (Table 4) with beam sizes of 14″, 12″, and 9″ in IRAS 03235, IRAS 03245, and IRAS 03271. These beam sizes correspond to the size of the $HC_3N$ emission in its moment 0 maps. In the IRAS 03235 and IRAS 03271 panels of Figure 4, blue lines indicate velocity positions of 5.4 and 5.7 km s$^{-1}$, which are the $V_{LSR}$ values of $HC_3N$ in each source.

We analyzed spectra using the CASSIS software (Caux et al. 2011). In the analyses, we used the local thermodynamic equilibrium (LTE) model available in the CASSIS spectrum analyzer, assuming that the lines are optically thin. Using the Markov Chain Monte Carlo (MCMC) method and the LTE model, we derived the column densities ($N$) and excitation temperatures ($T_{ex}$) of $HC_3N$ and $CH_3OH$, treating $N$, $T_{ex}$, line width (FWHM), and $V_{LSR}$ as semi-free parameters within

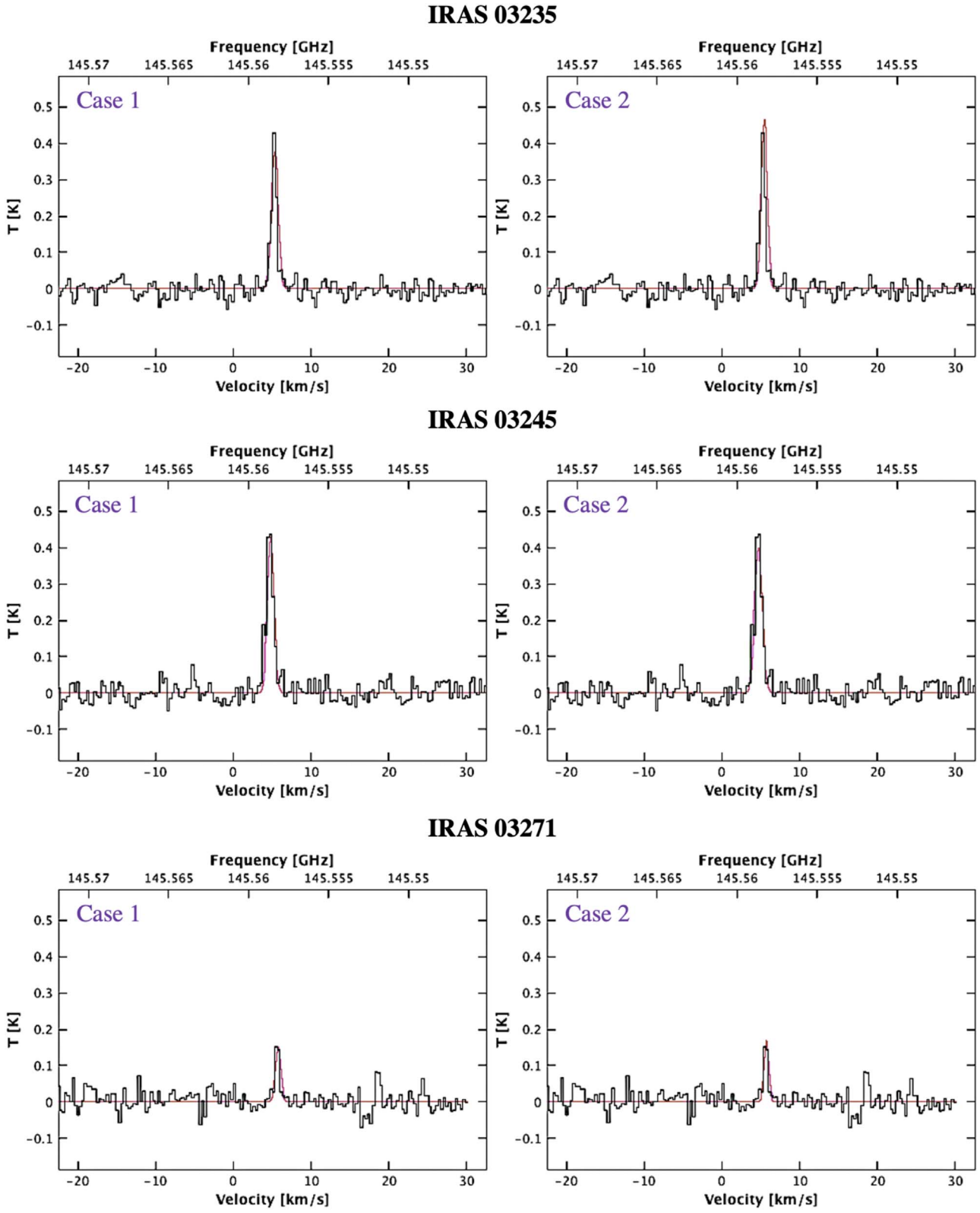


**Figure 3.** Spectra of $HC_3N$ ($J = 16 - 15$) toward the positions of peak emission of this molecule. The purple lines are modeled spectra of the best fitted results with CASSIS.

certain ranges. In the MCMC method, the minimum and maximum values set for parameter in a component define the bounds in which the values are chosen randomly. We consider the following two cases:

1. The range of the excitation temperature of both $HC_3N$ and $CH_3OH$ is 15–30 K; hereafter Case 1.
2. The excitation temperatures are comparable to dust temperatures (Table 1); the excitation temperature ranges

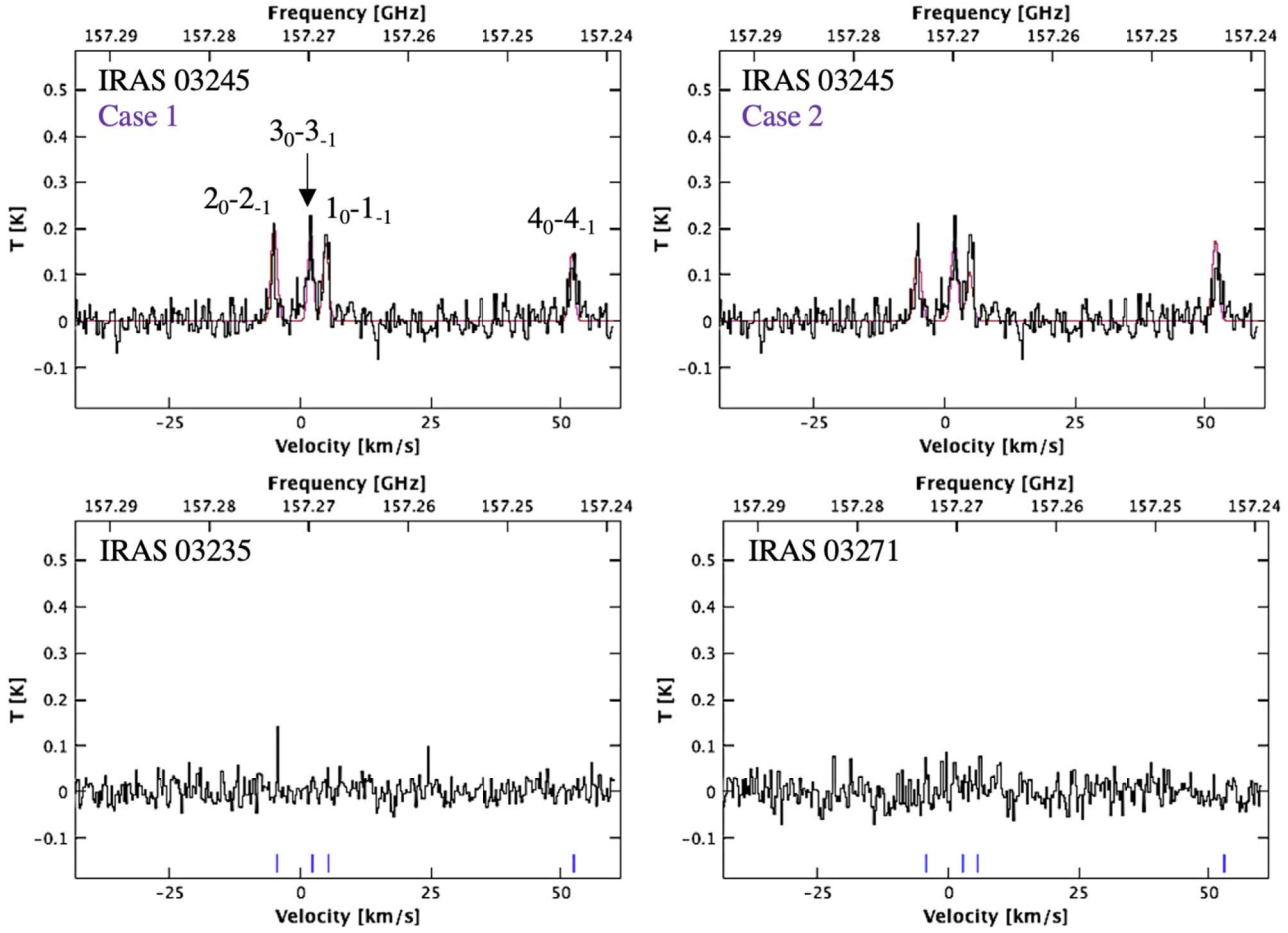


**Figure 4.** Spectra of $CH_3OH$ ($4_0 - 4_{-1}$ $E_2$, $1_0 - 1_{-1}$ $E_2$, $3_0 - 3_{-1}$ $E_2$, and $2_0 - 2_{-1}$ $E_2$) at the $HC_3N$ emission peaks. The purple lines are modeled spectra of the best fitted results with CASSIS. In panels of IRAS 03235 and IRAS 03271, the blue lines indicate the positions of the $CH_3OH$ lines with the same $V_{LSR}$ values as those of $HC_3N$, 5.4 and 5.7 km s$^{-1}$ for panels of IRAS 03235 and IRAS 03271, respectively.

are set at 35–40 K in IRAS 03235 and IRAS 03245, and 35–50 K in IRAS 03271 (Case 2).

We consider the first case because the WCCC mechanism (Sakai & Yamamoto 2013) seems to work in our target sources as mentioned in Section 3.1. The assumed temperature range covers typical excitation temperatures of carbon-chain species in L1527 (Yoshida et al. 2019). We adopt the second case because the observed lines may come from inner dense cores compared with previous single-dish observations (Graninger et al. 2016a; Bergner et al. 2017; Yoshida et al. 2019), where contributions from outer envelopes may be significant due to low upper-state-energy lines, and the excitation temperature may be underestimated in our data.

The obtained parameters for each case are summarized in Table 5. The modeled spectra using the best fitted values are overlaid as purple lines in Figures 3 and 4. The line widths (FWHM) of $HC_3N$ in our target sources ($\sim$1 km s$^{-1}$) are larger than the typical value in starless cores ($\sim$0.5 km s$^{-1}$; Kaifu et al. 2004) but similar to that in the L1527 low-mass WCCC source (Yoshida et al. 2019). Thus, the detected $HC_3N$ line seems to mainly trace lukewarm regions and not come from outer cold regions. In IRAS 03245, the $V_{LSR}$ value of $HC_3N$ is consistent with that of $CH_3OH$.

The obtained excitation temperatures of $HC_3N$ in all of the three sources in Case 1 are 16–18 K, which are comparable with those in L1527 (Yoshida et al. 2019). The derived column densities of $HC_3N$ change by only a factor of $\sim$3–4 between Cases 1 and 2. The column densities of $HC_3N$ in Case 1 are slightly higher than the previous results obtained with the IRAM 30 m telescope (the telescope beam size is $\sim$25″; Bergner et al. 2017) by a factor of $\approx$1.3–2. Bergner et al. (2017) derived the $HC_3N$ column densities by the rotational diagram method using the two lines with almost similar upper-state energies or using only one line with assumed fixed rotational temperatures. The effect of the beam dilution could also result in the lower column densities in the single-dish observations (Bergner et al. 2017).

The $CH_3OH$ column densities in IRAS 03245 for Cases 1 and 2 are higher than that derived by Graninger et al. (2016b) by a factor of 1.8–2.8. Graninger et al. (2016b) derived the $CH_3OH$ column density to be $(1.5 \pm 0.3) \times 10^{13}$ cm$^{-2}$ from observations with the IRAM 30 m telescope. Again, this difference in column density could be caused by the beam dilution in the single-dish observations.

## 4. Discussion

We now compare the derived $CH_3OH/HC_3N$ column-density ratios with those derived by the chemical network simulations. We describe our chemical network simulations in Section 4.1, and compare observations and simulations in Section 4.2.

**Table 5**
Obtained Parameters from the Spectral Analyses

| Source | Species | Case 1 | | | | Case 2 | | | |
|---|---|---|---|---|---|---|---|---|---|
| | | $N$ ($cm^{-2}$) | $T_{ex}$ (K) | FWHM (km $s^{-1}$) | $V_{LSR}$ (km $s^{-1}$) | $N$ ($cm^{-2}$) | $T_{ex}$ (K) | FWHM (km $s^{-1}$) | $V_{LSR}$ (km $s^{-1}$) |
| IRAS 03235 | $HC_3N$ | $(4.9 \pm 0.4) \times 10^{12}$ | $18.0 \pm 0.9$ | $1.06 \pm 0.05$ | $5.38 \pm 0.02$ | $(1.3 \pm 0.7) \times 10^{12}$ | $37.3 \pm 0.2$ | $0.83 \pm 0.06$ | $5.43 \pm 0.02$ |
| IRAS 03245 | $HC_3N$ | $(7.2 \pm 0.2) \times 10^{12}$ | $16.3 \pm 0.4$ | $0.989 \pm 0.006$ | $4.821 \pm 0.017$ | $(2.7 \pm 1.1) \times 10^{12}$ | $37.3 \pm 0.3$ | $1.05 \pm 0.07$ | $4.72 \pm 0.05$ |
| | $CH_3OH$ | $(2.7 \pm 0.4) \times 10^{13}$ | $17.5 \pm 0.4$ | $1.30 \pm 0.13$ | $4.86 \pm 0.05$ | $(4.3 \pm 0.5) \times 10^{13}$ | $37.4 \pm 1.5$ | $1.50 \pm 0.17$ | $4.74 \pm 0.04$ |
| IRAS 03271 | $HC_3N$ | $(2.2 \pm 0.3) \times 10^{12}$ | $16.2 \pm 0.8$ | $0.82 \pm 0.11$ | $5.745 \pm 0.012$ | $(5.3 \pm 1.6) \times 10^{11}$ | $46.6 \pm 1.6$ | $0.71 \pm 0.16$ | $5.72 \pm 0.04$ |

**Note.** The errors represent the standard deviation.

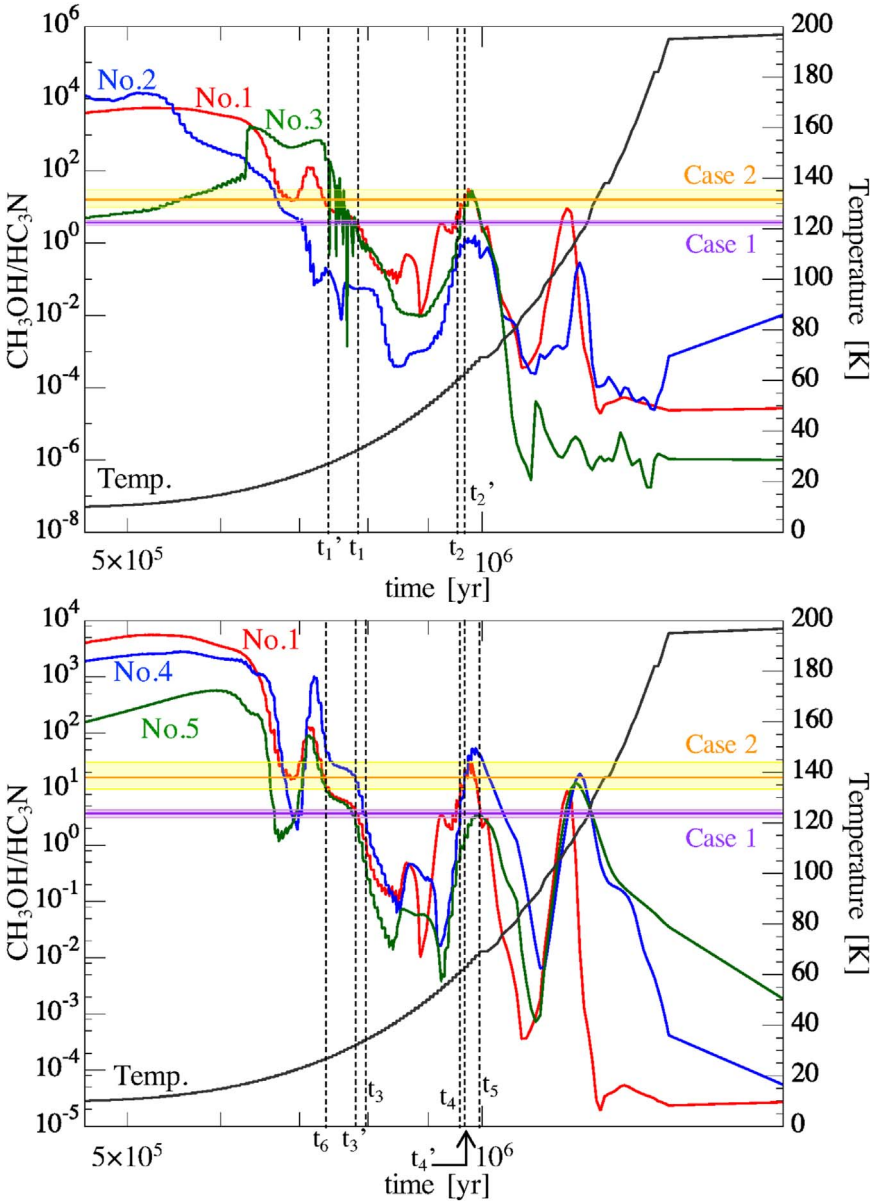


**Figure 5.** Comparisons of the $CH_3OH/HC_3N$ ratios between observations and chemical network simulations (Models No. 1–No. 5, see Table 6). The purple and orange horizontal lines indicate the observed values in IRAS 03245 for Case 1 and Case 2, respectively. The black curves indicate gas (and dust) temperature evolution from the model. The symbols of $t_n$ and $t_n'$, ($n$ = 1–6) associated with dashed vertical lines represent the ages when the observed $CH_3OH/HC_3N$ ratios agree with the modeled values. The details are described in the main text and values are summarized in Table 7.

**Table 6**
Summary of Models

| Model | $\zeta$ ($s^{-1}$)[a] | C/O Ratio |
|---|---|---|
| No. 1 | $1.3 \times 10^{-17}$ | 0.4[b] |
| No. 2 | $3.0 \times 10^{-16}$ | 0.4[b] |
| No. 3 | $4.0 \times 10^{-14}$ | 0.4[b] |
| No. 4 | $1.3 \times 10^{-17}$ | 0.5[c] |
| No. 5 | $1.3 \times 10^{-17}$ | 1.2[d] |

**Notes.**
[a] Cosmic-ray ionization rates used in the model
[b] The C/O ratio of 0.4 corresponds to $C^+ = 7.3 \times 10^{-5}$ and $O = 1.76 \times 10^{-4}$, and the rest of the elemental abundances remain the same as described in Taniguchi et al. (2019a).
[c] Corresponding to $C^+ = 1.7 \times 10^{-4}$ and $O = 3.3 \times 10^{-4}$.
[d] Corresponding to $C^+ = 1.7 \times 10^{-4}$ and $O = 1.4 \times 10^{-4}$.

### 4.1. Chemical Network Simulations

We used the chemical network code Nautilus (Ruaud et al. 2016) and a hot-core model with a warm-up stage. The physical evolution is the same as that in Taniguchi et al. (2019a). The initial gas density is $n_H = 10^4$ cm$^{-3}$ and increases to $10^7$ cm$^{-3}$ during the freefall collapse. The initial temperature is 10 K and rises to 200 K during the warm-up period. In this paper, we investigated low-mass YSOs, and thus we utilized the model with a slow warm-up period ($1 \times 10^6$ yr). The dust temperature is assumed to be equal to the gas temperature.

We changed the cosmic-ray ionization rate ($\zeta$) and the initial C/O ratio in order to investigate the dependence of the $CH_3OH/HC_3N$ ratio on these parameters. Table 6 summarizes the models used in this paper. Models No. 1–No. 3 are the same as those presented in Taniguchi et al. (2019a). The C/O elemental ratio could change the $CH_3OH$ and $HC_3N$

abundances. We included the high cosmic-ray ionization rates because this rate ($\zeta = 4.0 \times 10^{-14}$ s$^{-1}$) can reproduce the observed abundances of carbon-chain species in intermediate-mass protoclusters (Fontani et al. 2017; Favre et al. 2018) and around some massive young stellar objects (MYSOs; Taniguchi et al. 2019a, 2021).

Figure 5 shows the time dependence of the $CH_3OH/HC_3N$ ratio during the warm-up period, taking the evolutionary stages of our target sources into consideration. As a general trend of these models, the $CH_3OH/HC_3N$ ratio decreases after $\sim 7 \times 10^5$ yr ($23\ \mathrm{K} < T < 50\ \mathrm{K}$), slightly increases during $\sim 9 \times 10^5$–$10^6$ yr ($50\ \mathrm{K} < T < 70\ \mathrm{K}$), and then drops again. Such complicated features are caused by combinations of the temporal or thermal dependence of the abundance of $CH_3OH$ and $HC_3N$ during the warm-up stage.

The formation pathways of $HC_3N$ during the warm-up stage are discussed in detail in Taniguchi et al. (2019a) and we include only a short description here. Methane ($CH_4$) desorbs from ice mantles at temperatures above 25 K, and rapidly starts forming carbon-chain species in the gas phase, via the WCCC mechanism (Hassel et al. 2008). This explains the first decrease in the $CH_3OH/HC_3N$ ratio, because there is no efficient formation pathway for the gas-phase $CH_3OH$ at that time ($T \approx 25$–$50$ K, $t \approx 7.2 \times 10^5$–$9 \times 10^5$ yr). After $HC_3N$ is formed in the gas phase, it is soon adsorbed onto dust grains and accumulated in ice mantles, leading to a decrease in the gas-phase $HC_3N$ abundance.

Methanol ($CH_3OH$) is mainly formed by the electron recombination reaction of $CH_3OCH_4^+$ ($t \approx 7 \times 10^5$–$10^6$ yr) in the gas phase, before the temperature reaches its sublimation temperature. The formation of the $CH_3OCH_4^+$ ion becomes enhanced by the reaction between $HCO^+$ and $CH_3OCH_3$, for which the formation increases in rate by the associative gas-phase reaction between $CH_3O$ and $CH_3$ from $t \approx 7 \times 10^5$ yr.

After the temperature reaches 87 K ($t = 1.09 \times 10^6$ yr), $CH_3OH$ desorbs from dust grains and its gas-phase abundance increases sharply, while $HC_3N$ starts desorbing from dust grains at $t \simeq 1.1 \times 10^6$ yr ($T \simeq 90$, K).

### 4.2. Comparison of the $CH_3OH/HC_3N$ Abundance Ratio between Observations and Models

The observed $CH_3OH/HC_3N$ ratios in IRAS 03245 are derived to be $3.7 \pm 0.6$ and $16^{+14}_{-6}$ for Case 1 and Case 2, respectively, using the results summarized in Table 5. The upper panel of Figure 5 shows the time dependence of the $CH_3OH/HC_3N$ ratio for three models with different cosmic-ray ionization rates (Models No. 1–No. 3), while the lower panel shows three models with different C/O ratios (Models No. 1, No. 4, and No. 5). The observed $CH_3OH/HC_3N$ ratios are indicated as horizontal lines including error bars; purple and orange lines indicate the results of Case 1 and Case 2, respectively. The temperature scale arises from only the model. We now focus on comparison with observations, starting with ages after the temperature reaches 25 K, at which the WCCC mechanism starts ($t \geqslant 7.2 \times 10^5$ yr).

We first compare the observed ratio in IRAS 03245 to Model No. 1. The observed ratio for Case 1 ($3.7 \pm 0.6$) agrees with Model No. 1 at $t \approx 7.8 \times 10^5$ yr (labeled as $t_1$), at which the temperature is $\simeq$32 K, as shown in the upper panel of Figure 5. This dust temperature agrees with the dust temperature derived in IRAS 03245 ($37 \pm 2$ K; Emprechtinger et al. 2009, see also Table 1 in this paper). Around $t \approx (9.2$–$9.3) \times 10^5$ yr ($t_2$, $T \approx 55$ K), the observed ratio in IRAS 03245 again agrees with Model No. 1, but the temperature is slightly higher than the dust temperature in IRAS 03245.

The observed ratio in IRAS 03245 with Case 2 ($16^{+14}_{-6}$) is consistent with Model No. 1 around $(7.3$–$7.5) \times 10^5$ yr ($t_1$', $T \simeq 26$–$28$ K). The dust temperature of 26–28 K is slightly lower than the observed dust temperature in this source. Since we assumed that the higher temperature conditions in Case 2 compared with Case 1 and the excitation temperatures of $HC_3N$ and $CH_3OH$ are derived to be around 37 K in Case 2 (Table 5), such a lower temperature (26–28 K) compared to Case 1 ($\simeq$32 K) is contradictory. Besides, the $CH_3OH/HC_3N$ ratio with Case 2 agrees with Model No. 1 around $(9.6$–$9.7) \times 10^5$ yr ($t_2'$, 62–65 K). However, the temperature at this age is higher than the observed dust temperature in this source.

In a similar manner, we investigate the ages and temperatures when the observed $CH_3OH/HC_3N$ ratios match those derived by other models (No. 2–No. 5), and the results are summarized in Table 7. In Model No. 2, the modeled $CH_3OH/HC_3N$ ratio is lower than the observed ratios in IRAS 03245 for Cases 1 and 2 after $t \geqslant 7.2 \times 10^5$ yr, so that Model No. 2 cannot reproduce the observed ratio in this source.

Taking all of the results summarized in Table 7 into consideration, the observed $CH_3OH/HC_3N$ column-density ratio and dust temperature in IRAS 03245 can be best reproduced simultaneously by our models at $t \approx (7.7$–$7.9) \times 10^5$ yr ($T \approx 31$–$34$ K). This temperature range agrees with the WCCC mechanism (Hassel et al. 2008). The other temperature ranges ($\sim$25–28 K and $\sim$60–70 K) are not consistent with the observed dust temperatures, and hence these ages and temperatures are unlikely.

In IRAS 03235 and IRAS 03271, we could not detect $CH_3OH$, and the $CH_3OH/HC_3N$ ratio should be lower than that in IRAS 03245 ($<3.7$). In that case, the $CH_3OH/HC_3N$ ratios toward these two low-mass YSOs agree with Model No. 1 around $t_1 (7.8 \times 10^5\ \mathrm{yr}) < t < t_2 (9.3 \times 10^5\ \mathrm{yr})$, corresponding to $32\ \mathrm{K} < T < 55\ \mathrm{K}$. Although the dust temperature was not derived in IRAS 03235, it is expected that it is not so far from those in IRAS 03245 ($37 \pm 2$ K) and IRAS 03271 ($45 \pm 2$ K) because of their similar ages and physical properties (see Table 1). If this is the case, the suggested temperature range agrees with the dust temperatures in IRAS 03235 and IRAS 03271. In the model calculations, the $CH_3OH/HC_3N$ ratios become lower than the observed ratios in IRAS 03245 after $\approx 10^6$ yr. However, the dust temperature becomes higher than 70 K after $\approx 10^6$ yr. These dust temperatures above 70 K

**Table 7**
Summary of Ages at Which Models Agree with the Observed $CH_3OH/HC_3N$ Ratio and Corresponding Temperatures

| Label | Age (yr) | Temperature (K) | Pair of Model and Observation |
|---|---|---|---|
| $t_1$ | $7.8 \times 10^5$ | 32 | No. 1, 3, 5 & Case 1 |
| $t_2$ | $(9.2$–$9.3) \times 10^5$ | 55 | No. 1, 3 & Case 1 |
| $t_1'$ | $(7.3$–$7.5) \times 10^5$ | 26–28 | No. 1, 3 & Case 2 |
| $t_2'$ | $(9.6$–$9.7) \times 10^5$ | 62–65 | No. 1, 3 & Case 2 |
| $t_3$ | $7.9 \times 10^5$ | 34 | No. 4 & Case 1 |
| $t_4$ | $9.5 \times 10^5$ | 60 | No. 4 & Case 1 |
| $t_3$' | $(7.7$–$7.8) \times 10^5$ | 31–33 | No. 4 & Case 2 |
| $t_4$' | $9.7 \times 10^5$ | 63 | No. 4 & Case 2 |
| $t_5$ | $(9.8$–$10) \times 10^5$ | 66-69 | No. 5 & Case 1 |
| $t_6$ | $7.3 \times 10^5$ | 26 | No. 5 & Case 2 |

are not consistent with the observed dust temperatures in our target sources. Thus, we omit a possibility of ages after $\approx 10^6$ yr.

Since the dust temperatures in the observed sources do not reach the sublimation temperature of $CH_3OH$, we conclude that the nonthermal desorption mechanisms or gas-phase formation reactions leading to $CH_3OH$ are the primary contributors to gas-phase $CH_3OH$ formation around low-mass Class 0 and Class I YSOs at the time/temperature regime studied here. These mechanisms seem to be especially efficient in IRAS 03245, among the observed three sources. In the chemical network simulation, gas-phase ion-molecule reactions contribute to the formation of gas-phase $CH_3OH$, via the electron recombination reaction of $CH_3OCH_4^+$. These hypotheses for gas-phase $CH_3OH$ formation, in particular those involving nonthermal desorption such as photodesorption, are supported by the fact that the bolometric luminosity in IRAS 03245 is higher than the other two sources.

## 5. Conclusions

We have analyzed ALMA Cycle 5 data in Band 4 toward three low-mass YSOs: IRAS 03235+3004 (IRAS 03235), IRAS 03245+3002 (IRAS 03245), and IRAS 03271+3013 (IRAS 03271), in the Perseus region. The $HC_3N$ ($J = 16 - 15$) line was detected toward all sources, while the $CH_3OH$ lines were detected only toward IRAS 03245. The detection/nondetection of $CH_3OH$ is independent of the mass of envelopes. These results may imply the chemical diversity around low-mass YSOs.

In IRAS 03235 and IRAS 03245, both of which are Class 0 sources, the continuum peaks correspond to the Spitzer sources. The spatial distributions of $HC_3N$ are extended relative to those of the continuum emission in these two sources. On the other hand, the spatial distribution of $CH_3OH$ matches the continuum emission in IRAS 03245. In IRAS 03271, the spatial distribution of the continuum emission shows an elongated feature and its peak does not correspond to the Spitzer source. The spatial distribution of $HC_3N$ differs from that of continuum emission and its peak does not match with the Spitzer source. Although we could not understand the discrepancy between the spatial distributions of $HC_3N$ and that of continuum with the current angular resolution, $HC_3N$ may have originated from the molecular outflow.

We derived the column densities and excitation temperatures of $HC_3N$ and $CH_3OH$ with the CASSIS software. The $CH_3OH/HC_3N$ ratio in IRAS 03245 was derived to be $3.7 \pm 0.6$ and $16^{+14}_{-6}$ on the assumptions that the excitation temperature is close to that of L1527, and the excitation temperature is close to the dust temperatures, respectively. We compared the observed $CH_3OH/HC_3N$ ratios to those derived by the chemical network simulations. The observed $CH_3OH/HC_3N$ ratios in IRAS 03245 are reproduced at ages when the dust temperatures lie around ≈30–35 K, which agrees with the dust temperature in IRAS 03245. Regarding the other two sources, where $CH_3OH$ has not been detected, the $CH_3OH/HC_3N$ ratios, which should be lower than that in IRAS 03245, can be reproduced when the temperatures lie between $32\,\mathrm{K} < T < 55\,\mathrm{K}$, which agrees with the dust temperatures in these low-mass YSOs.

At the times when the observed $CH_3OH/HC_3N$ ratios and the dust temperatures are reproduced, $HC_3N$ is efficiently formed by the WCCC mechanism. The nonthermal desorption or sublimation or the gas-phase reactions contribute to the formation of gas-phase $CH_3OH$ during the times. The higher bolometric luminosity in IRAS 03245 seems to support these conclusions, especially the importance of nonthermal desorption mechanisms.

This paper makes use of the following ALMA data: ADS/JAO.ALMA#2017.1.00955.S. ALMA is a partnership of ESO (representing its member states), NSF (USA) and NINS (Japan), together with NRC (Canada), MOST and ASIAA (Taiwan), and KASI (Republic of Korea), in cooperation with the Republic of Chile. The Joint ALMA Observatory is operated by ESO, AUI/NRAO, and NAOJ. Based on analyses carried out with the CASSIS software and JPL spectroscopic database. CASSIS has been developed by IRAP-UPS/CNRS (http://cassis.irap.omp.eu). This work was supported by JSPS KAKENHI grant No. JP20K14523. This research was carried out in part at the Jet Propulsion Laboratory, which is operated for NASA by the California Institute of Technology. E.H. thanks the National Science Foundation for support through grant AST-1906489. S.T. is supported by JSPS KAKENHI Grant no. 18K03703. We thank the anonymous referee who gave us valuable comments, which helped us improve the quality of the paper.

*Facility:* Atacama Large Millimeter/submillimeter Array (ALMA).

*Software:* Common Astronomy Software Applications package (CASA; McMullin et al. 2007), CASSIS (Caux et al. 2011), Nautilus (Ruaud et al. 2016).

## ORCID iDs

Kotomi Taniguchi https://orcid.org/0000-0003-4402-6475
Liton Majumdar https://orcid.org/0000-0001-7031-8039
Shigehisa Takakuwa https://orcid.org/0000-0003-0845-128X
Masao Saito https://orcid.org/0000-0003-0769-8627
Dariusz C. Lis https://orcid.org/0000-0002-0500-4700
Paul F. Goldsmith https://orcid.org/0000-0002-6622-8396
Eric Herbst https://orcid.org/0000-0002-4649-2536

## References

Acharyya, K., & Herbst, E. 2017, ApJ, 850, 105
Balucani, N., Ceccarelli, C., & Taquet, V. 2015, MNRAS, 449, L16
Bergner, J. B., Guzmán, V. G., Öberg, K. I., et al. 2018, ApJ, 857, 69
Bergner, J. B., Öberg, K. I., Garrod, R. T., et al. 2017, ApJ, 841, 120
Caselli, P., & Ceccarelli, C. 2012, A&ARv, 20, 56
Caux, E., Bottinelli, S., Vastel, C., et al. 2011, in IAU Symp. 280, The Molecular Universe, 280 (Cambridge: Cambridge Univ. Press), 120
Ceccarelli, C. 2004, in ASP Conf. Proc. 323, Star Formation in the Interstellar Medium: In Honor of David Hollenbach, 323, ed. D. Johnson et al. (San Francisco, CA: ASP), 195
Dunham, M. M., Allen, L. E., Evans, N. J., et al. 2015, ApJS, 220, 11
Emprechtinger, M., Caselli, P., Volgenau, N. H., et al. 2009, A&A, 493, 89
Enoch, M. L., Evans, N. J., Sargent, A. I., et al. 2009, ApJ, 692, 973
Evans, N. J., Allen, L. E., Blake, G. A., et al. 2003, PASP, 115, 965
Favre, C., Ceccarelli, C., López-Sepulcre, A., et al. 2018, ApJ, 859, 136
Fontani, F., Ceccarelli, C., Favre, C., et al. 2017, A&A, 605, A57
Graninger, D. M., Wilkins, O. H., & Öberg, K. I. 2016a, ApJ, 819, 140
Graninger, D. M., Wilkins, O. H., & Öberg, K. I. 2016b, ApJ, 833, 125
Hassel, G. E., Herbst, E., & Garrod, R. T. 2008, ApJ, 681, 1385
Herbst, E., & van Dishoeck, E. F. 2009, ARA&A, 47, 427
Hsieh, T.-H., Murillo, N. M., Belloche, A., et al. 2019, ApJ, 884, 149
Jiménez-Serra, I., Vasyunin, A. I., Caselli, P., et al. 2016, ApJL, 830, L6
Jin, M., & Garrod, R. T. 2020, ApJS, 249, 26
Jørgensen, J. K., Belloche, A., & Garrod, R. T. 2020, ARA&A, 58, 727
Kaifu, N., Ohishi, M., Kawaguchi, K., et al. 2004, PASJ, 56, 69

Law, C. J., Öberg, K. I., Bergner, J. B., et al. 2018, ApJ, 863, 88
Maureira, M. J., Arce, H. G., Dunham, M. M., et al. 2020, MNRAS, 499, 4394
McMullin, J. P., Waters, B., Schiebel, D., et al. 2007, in ASP Conf. Ser. 376, Astronomical Data Analysis Software and Systems XVI, 376, ed. R. A. Shaw et al. (San Francisco, CA: ASP), 127
Öberg, K. I., & Bergin, E. A. 2021, PhR, 893, 1
Öberg, K. I., Guzmán, V. V., Furuya, K., et al. 2015, Natur, 520, 198
Ortiz-León, G. N., Loinard, L., Dzib, S. A., et al. 2018, ApJ, 865, 73
Paulive, A., Shingledecker, C. N., & Herbst, E. 2021, MNRAS, 500, 3414
Pickett, H. M., Poynter, R. L., Cohen, E. A., et al. 1998, JQSRT, 60, 883
Ruaud, M., Wakelam, V., & Hersant, F. 2016, MNRAS, 459, 3756
Sakai, N., Sakai, T., Hirota, T., et al. 2010, ApJ, 722, 1633
Sakai, N., & Yamamoto, S. 2013, ChRv, 113, 8981
Scibelli, S., & Shirley, Y. 2020, ApJ, 891, 73
Shingledecker, C. N., & Herbst, E. 2018, PCCP, 20, 5359
Shingledecker, C. N., Tennis, J., Le Gal, R., et al. 2018, ApJ, 861, 20
Spezzano, S., Bizzocchi, L., Caselli, P., et al. 2016, A&A, 592, L11
Suzuki, H., Yamamoto, S., Ohishi, M., et al. 1992, ApJ, 392, 551
Takakuwa, S., Kamazaki, T., Saito, M., et al. 2003a, ApJ, 584, 818
Takakuwa, S., Mikami, H., & Saito, M. 1998, ApJ, 501, 723
Takakuwa, S., Mikami, H., Saito, M., et al. 2000, ApJ, 542, 367
Takakuwa, S., Ohashi, N., & Hirano, N. 2003b, ApJ, 590, 932
Taniguchi, K., Herbst, E., Caselli, P., et al. 2019a, ApJ, 881, 57
Taniguchi, K., Herbst, E., Majumdar, L., et al. 2021, ApJ, 908, 100
Taniguchi, K., Plunkett, A., Herbst, E., et al. 2020, MNRAS, 493, 2395
Taniguchi, K., Saito, M., Sridharan, T. K., et al. 2018, ApJ, 854, 133
Taniguchi, K., Saito, M., Sridharan, T. K., et al. 2019b, ApJ, 872, 154
Taquet, V., Wirström, E. S., Charnley, S. B., et al. 2017, A&A, 607, A20
White, G. J., Fridlund, C. W. M., Bergman, P., et al. 2006, ApJL, 651, L41
Yoshida, K., Sakai, N., Nishimura, Y., et al. 2019, PASJ, 71, S18